



OPEN

Reliability of fNIRS for noninvasive monitoring of brain function and emotion in sheep

Matteo Chincarini^{1,8}, Emanuela Dalla Costa^{2,8}, Lina Qiu^{3,4,8}, Lorenzo Spinelli⁵, Simona Cannas², Clara Palestrini², Elisabetta Canali², Michela Minero², Bruno Cozzi⁶, Nicola Ferri⁷, Daniele Ancora³, Francesco De Pasquale¹, Giorgio Vignola¹ & Alessandro Torricelli^{3,5}✉

The aim of this work was to critically assess if functional near infrared spectroscopy (fNIRS) can be profitably used as a tool for noninvasive recording of brain functions and emotions in sheep. We considered an experimental design including advances in instrumentation (customized wireless multi-distance fNIRS system), more accurate physical modelling (two-layer model for photon diffusion and 3D Monte Carlo simulations), support from neuroanatomical tools (positioning of the fNIRS probe by MRI and DTI data of the very same animals), and rigorous protocols (motor task, startling test) for testing the behavioral response of freely moving sheep. Almost no hemodynamic response was found in the extra-cerebral region in both the motor task and the startling test. In the motor task, as expected we found a canonical hemodynamic response in the cerebral region when sheep were walking. In the startling test, the measured hemodynamic response in the cerebral region was mainly from movement. Overall, these results indicate that with the current setup and probe positioning we are primarily measuring the motor area of the sheep brain, and not probing the too deeply located cortical areas related to processing of emotions.

How animals are treated matters both to animals and to people. The focus on animal welfare stems from the recognition that animals are sentient beings and finding noninvasive indicators of animal emotion and cognition processes is an important goal in disciplines ranging from neuroscience to animal welfare. However, the neurophysiological basis of behavior of domestic herbivores, raised for meat, milk or wool production, are still largely unknown. The sheep may be adapted as a valid model for its ability to perform a variety of complex tasks and behaviors involving goal-oriented motor coordination, emotion, facial recognition and memory-based performance^{1–4}. In addition, the convoluted brain of the sheep may be considered as an alternative to rodents in translational experimental neuroscience^{1,5}. As cognitive processes or emotional states can often be reflected in brain responses⁶, a better understanding of affective states of sheep in various environments or as a response to different stimuli will benefit both neuroscience and animal welfare.

Understanding how cognitive processes and emotional states are expressed in animal brain is still a challenge, especially in a noninvasive manner. Previously, several methods successfully used in human brain mapping have been employed in functional imaging of the animal brain, including functional magnetic resonance imaging (fMRI)^{7–14}, electroencephalography and sensory evoked potentials^{15–19}. While in human studies tasks and stimuli can be presented to an awake and collaborating subject, most measurement techniques require the animal to be under anesthesia. Therefore, its brain response can be strongly affected.

Functional near-infrared spectroscopy (fNIRS) is a novel technique that employs near-infrared light to non-invasively measure the concentration of oxygenated hemoglobin [O₂Hb] and deoxygenated hemoglobin [HHb]

¹Facoltà Di Medicina Veterinaria, Università Degli Studi Di Teramo, Teramo, Italy. ²Dipartimento Di Medicina Veterinaria, Università Degli Studi Di Milano, Milan, Italy. ³Dipartimento Di Fisica, Politecnico Di Milano, Milan, Italy. ⁴School of Software, South China Normal University, Guangzhou, China. ⁵Istituto Di Fotonica E Nanotecnologie, Consiglio Nazionale Delle Ricerche, Milan, Italy. ⁶Dipartimento Di Biomedicina Comparata E Alimentazione, Università Degli Studi Di Padova, Padova, Italy. ⁷Istituto Zooprofilattico Sperimentale Dell'Abruzzo E del Molise G. Caporale, Teramo, Italy. ⁸These authors contributed equally: Matteo Chincarini, Emanuela Dalla Costa and Lina Qiu. ✉email: alessandro.torricelli@polimi.it

in cerebral human tissue, or typically their changes with respect to a baseline period, $[\Delta\text{O}_2\text{Hb}]$ and $[\Delta\text{HHb}]$. Like fMRI, fNIRS relies on the neurovascular coupling mechanism²⁰, and on the ability of near-infrared light to penetrate deeply in biological tissue²¹. Being non-invasive, safe, portable, and characterized by a low susceptibility to motion artifacts, fNIRS has been widely and successfully employed in human studies²². The most commonly utilized fNIRS approach is the continuous wave fNIRS (CW-fNIRS) employing steady state light sources and detectors²¹. Since CW-fNIRS systems can be wireless and miniaturized, several applications have also been carried out in free-moving domestic animals, e.g. goats²³, dogs²⁴, and sheep^{25–29}. In these studies, fNIRS monitoring has been considered and used as an additional technique to measure emotional and cognitive responses in animals exposed to different stimuli or different environments. Noticeably, results were sometimes inconsistent among studies^{6,30}, suggesting that measurement accuracy and reliability need to be improved.

As a matter of fact, all previous studies on farm animals^{23–29} employed a fNIRS system that was designed for human neonatology and not optimized for species-specific animal anatomy³¹. In particular, they all made use of a fixed configuration of source detector pairs with short (15 mm) and long (25 mm) acquisition channels that are sub-optimal for sampling cortical region and for discriminating extra-cerebral regions (i.e. scalp, skull and CSF) in animals like sheep with an average depth from scalp to brain cortex that can be up to 10 mm³², much closer to adult than to neonate humans.

Further, differently from what it is normally done in fNIRS studies on humans where probe placement can be guided by proper neuro-anatomical images and functional atlas^{33–35}, the placement of the probe on the animal head was not aided by magnetic resonance imaging (MRI) data and rarely it was not consistently supported by neuro-anatomical or functional atlas of the animal brain²⁵. Consequently, fNIRS signals were attributed to the frontal or pre-frontal region, also hypothesizing a vascular stealing mechanism in the brain cortex^{23,26–28}, but without determining the sensitivity of the technique to that specific cortical region.

Moreover, the methods employed for fNIRS data analysis potentially suffered from lack of accuracy. In fact, the more superficial hemodynamic events occurring in the scalp could interfere with the hemodynamic changes from the cortex unless a proper geometry method to model the head of the animal is adopted.

Finally, fNIRS data processing made use of a priori information on the differential pathlength factor (DPF) taken from the literature and obtained from a single dead animal³⁶. To improve accuracy of fNIRS data analysis, the DPF is in fact used to derive hemoglobin changes from the measured intensity changes by means of the Modified Beer Lambert law or similar model based approaches²¹. Wrong DPF data can yield to inaccurate estimates of hemoglobin concentration.

From the above observations, it becomes evident that the fNIRS technique is still an innovative, not fully validated approach for studying cortical activity in domestic animals. The aim of this work was to improve reliability and accuracy of fNIRS measurements in sheep and critically assess whether fNIRS can be profitably used as a tool for noninvasive recording of brain functions and emotions in this species. To this purpose we have considered an experimental design that encompasses advances in instrumentation (customized wireless multi-distance fNIRS system), more accurate physical modelling (two-layer model for photon diffusion and 3D Monte Carlo simulations), support from neuroanatomical tools (positioning of the fNIRS probe by MRI and DTI data of the very same animals), and rigorous protocols (motor task, startling test) for testing the behavioral response of freely moving sheep.

Results

Hemodynamic changes during the motor task. Out of the 13 sheep that performed the motor task, two sheep were excluded from the analysis because of frequent head shaking, as shown by the evaluation of the video recordings (for details on the ethogram see Supplementary Table ST2). In the remaining 11 sheep we calculated the group-average $[\Delta\text{O}_2\text{Hb}]$ and $[\Delta\text{HHb}]$ of the left and right hemispheres (Fig. 1, bottom row). The group-average in the two hemispheres shows a canonical hemodynamic response with an increase of $[\Delta\text{O}_2\text{Hb}]$ and a non symmetrical decrease in $[\Delta\text{HHb}]$ in the cerebral tissue during the movement ($p < 0.005$). Almost no hemodynamic changes were observed in the extra-cerebral tissue (Fig. 1 top row).

Hemodynamic changes during the startling test. Thirteen sheep underwent to the startling test, three of them were excluded due to their behavior during the task: two sheep showed frequent head shaking; one showed no no flight response or freezing after the umbrella opening. In the remaining 10 sheep we also excluded blocks if the animals were chewing or shaking the head. We thus retained approximately 80% of the recorded blocks (39 in total), that were then averaged to obtain the group-average $[\Delta\text{O}_2\text{Hb}]$ and $[\Delta\text{HHb}]$. In the extra-cerebral tissue there is almost no hemodynamic change throughout the test, as shown in Fig. 2, top row. In both hemispheres, the cerebral tissue showed a transient increase in $[\text{O}_2\text{Hb}]$ after the startle stimulus (as shown in Fig. 2, bottom row). Further, the right hemisphere also shows a transient classical brain activation pattern with increase in $[\text{O}_2\text{Hb}]$ and decrease in $[\text{HHb}]$.

Analysis of animal behavior revealed two distinct reactions to the startle stimulus: a flight response was observed in 28 blocks from 10 sheep, while freezing was observed in 11 blocks from 8 sheep. Therefore, we calculated the group-average $[\Delta\text{O}_2\text{Hb}]$ and $[\Delta\text{HHb}]$ for the two groups, labelled Move group and Stand group.

Both groups showed almost no hemodynamic response in the extra-cerebral tissue (Fig. 3 top row, and Fig. 4, top row). In the cerebral tissue, for the Move group (Fig. 3 bottom row) we have a canonical hemodynamic response (i.e. increase in $[\text{O}_2\text{Hb}]$ and decrease of $[\text{HHb}]$) in both left and right hemisphere. We also notice an increase in both oxygenated and deoxygenated hemoglobin in the left hemisphere cerebral tissue before the canonical response, during the opening of the umbrella, (see the gray area in Fig. 3 bottom row).

Conversely, for the Stand group the pattern of hemodynamic changes is less clear and different in the two hemispheres. In the left hemisphere we see a rapid increase of $[\text{O}_2\text{Hb}]$ and $[\text{HHb}]$ followed by a slow decay of

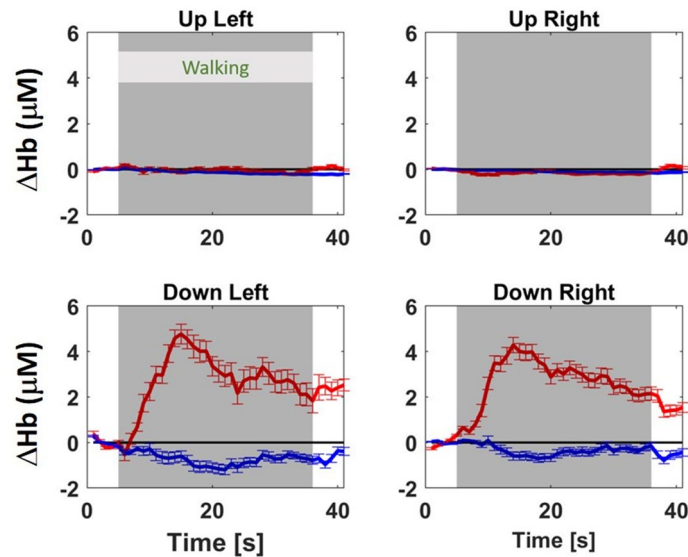


Figure 1. Group-average of $[\Delta O_2Hb]$ (red lines) and $[\Delta HHb]$ (blue lines), in μM , and their standard deviation during the motor task for extra-cerebral (up) tissue (top row) and cerebral (down) tissue (bottom row) and for the left (left column) and right (right column) hemisphere. In every plot, the first 5 s are the baseline (sheep stand still), followed by 30 s walking (marked as gray area), and finally 5 s recovery period (sheep stand still). The horizontal black line in every sub-figure indicates the zero value.

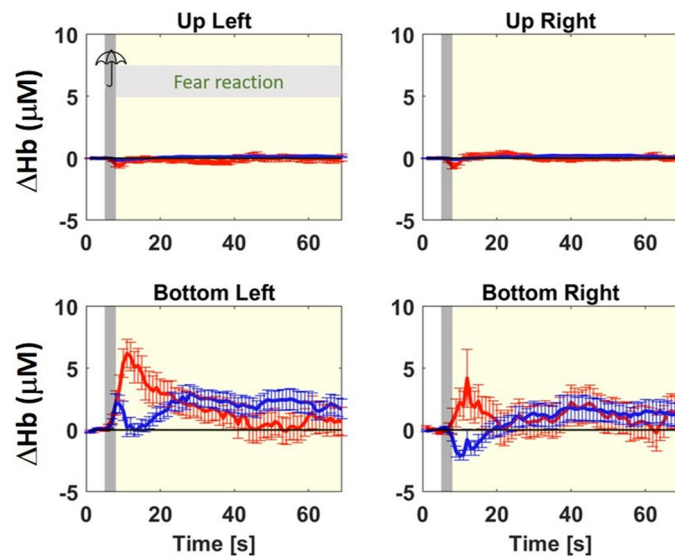


Figure 2. Group-average of $[\Delta O_2Hb]$ (red lines) and $[\Delta HHb]$ (blue lines), in μM , and their standard deviation during the startling test for extra-cerebral (up) tissue (top row) and cerebral (down) tissue (bottom row) and for the left (left column) and right (right column) hemisphere. In every subplot, the first 5 s is the baseline, followed by a 3 s startle stimulus (marked as gray area), and finally a 60 s fear reaction. The horizontal black line in every subplot indicates the zero value.

$[O_2Hb]$ to values smaller than the baseline, while for $[HHb]$ we observe a return to baseline values with a small undershoot (see Fig. 4, bottom left panel). In the right hemisphere after an initial decrease for both $[O_2Hb]$ and $[HHb]$, we notice a return to the baseline for $[HHb]$ and irregular oscillations for $[O_2Hb]$ that lead to values lower than the baseline (see Fig. 4, bottom right panel).

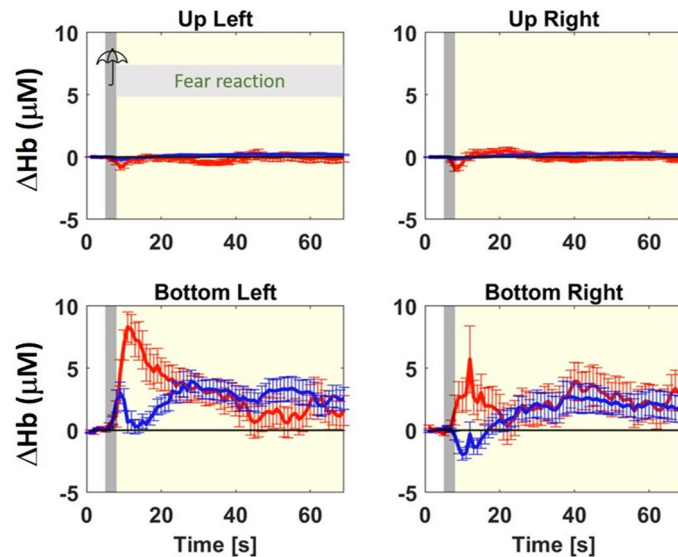


Figure 3. Same as Fig. 2 but group-average of the move group (sheep were moving during and after the 3 s startling stimulus).

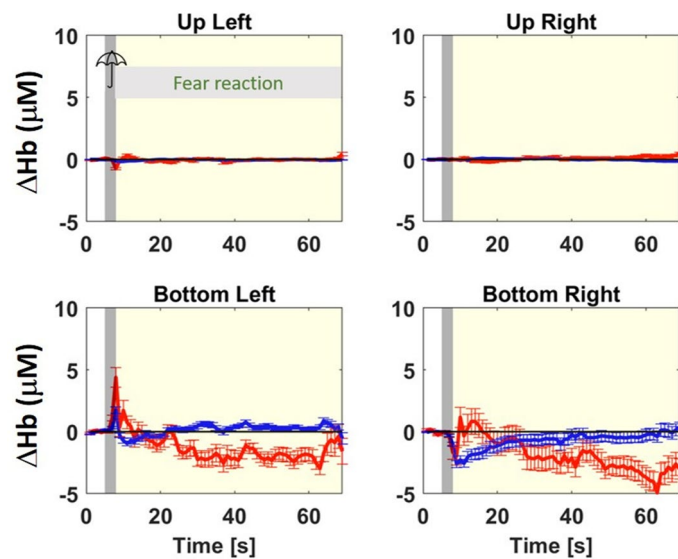


Figure 4. Same as Fig. 2 but group-average of the stand group (sheep were still during and after the 3 s startling stimulus).

Discussion

This study investigated the cerebral activity of freely moving sheep by using a wearable CW-fNIRS system applied to the animals performing a motor task and a startling test. Here we describe an experimental design that encompasses advances in instrumentation, more accurate physical modelling and rigorous protocols for assessing the animal behavioral response, with the aim of improving the fNIRS methodology applied to domestic animals.

Firstly, we employed a customized multi-distance wireless CW-fNIRS system with freely adaptable placement of sources and detectors. The short and long source-detector distances used were $\rho = 10$ mm and $\rho = 30$ mm, respectively. This configuration, notwithstanding the limitations imposed by the size and anatomical features of the animals' heads, allowed both to enhance photon penetration depth in the sheep head thanks to a long distance, longer than in previous studies, and to better discriminate extra- and intra-cerebral contributions, thanks to a reduced short distance. A study on the photon penetration depth at $\rho = 10$ mm and $\rho = 30$ mm in both simplified (homogeneous slab) and realistic (3D mesh from MRI data) geometry is reported in the Supplementary Section S3 to help the reader appreciate the different features of photon penetration at different distances.

We subsequently guided the positioning of the fNIRS probe by MRI data of the very same animals, since a neuro-anatomical and functional atlas for Sarda sheep (used in this study) was not available. We also checked the functional origin of the signal by diffusion tensor imaging (DTI) MRI on the animal brain. From MRI and

DTI data we confirmed that the location of the fNIRS probe was over the motor area of the cortex (see Supplementary Section S1).

Moreover, we noninvasively measured the optical properties (absorption coefficient and reduced scattering coefficient) of the head of all animals by employing a state-of-the-art multi-wavelength time-resolved diffuse spectroscopy system (see Supplementary Section S2). Photon distributions of time-of-flight (DTOF) were acquired at several wavelengths and fitted to a model for photon diffusion. Data of the optical properties were then used to improve a model-based data analysis. From the DTOF we also calculated the DPF on living sheep, therefore providing brand new data for this parameter (see Supplementary Table ST1). To the best of our current knowledge, the literature contains references only to post mortem DPF data obtained from a single animal³⁶. Our DPF data can contribute to enhancing the accuracy of analysis²¹ of other fNIRS studies enrolling sheep, thanks to the high uniformity that is expected from animal to animal due to genetic selection and reproduction procedures in animal production science^{37,38}.

Finally, to improve the estimate of the hemodynamic response in brain cortex, we have introduced, and validated by simulations (as reported in Supplementary Section S4), a model-based approach to data analysis of fNIRS signals from short and long distances. The model employs a two-layer geometry to better mimic the extra- and intra-cerebral tissue layers in the sheep's head, aiming at advancing the previous approaches based on a homogeneous model.

All the previously described activities were functional to the design of an experimental test capable of non-invasively estimate the cerebral hemodynamics of freely moving sheep during behavioral tasks. The motor task and the startling test were chosen as election assessments because (a) we wanted a straightforward test (the motor task) as a validation of our methodological approach; and (b) the startling test could give us insights into the possibility to monitor emotion and cognitive responses in sheep.

Before fNIRS recordings, sheep underwent a training period to minimize stress possibly associated with the tasks performance and behavioral reactions that could hamper the quality of fNIRS data acquisition³⁹. In particular, the sheep were habituated to be separated in small groups of animals of the same flock, to be handled by humans and to wear fake fNIRS devices (including cap, cables and chest straps). They were then trained to walk and stop in response to a vocal cue.

The results of the motor task were encouraging since a canonical hemodynamic response was observed, with increase in O₂Hb and decrease in HHb in the cortex located immediately below the fNIRS probe and without appreciable contribution from non-nervous tissues, including skin, subdermal layers, bone and dura mater. On the basis of the results of fNIRS experiments on human subjects where a similar hemodynamic response was found for motor task and walking experiments^{40,41}, we can conclude that the fNIRS technique with the proposed settings is able to monitor the cortical response associated to the execution of a motor task in sheep.

In the startling test, we found that—when moving during the startling stimulus (flight reaction)—the sheep showed a transient brain activation (i.e. increased hemodynamic response) that followed the actual stimulus. However, when the sheep was freezing, so remained standing still after the startle stimulus, the responses of both hemispheres were minimal, only showing a limited drop in [O₂Hb]. Even though the number of blocks of sheep showing a freezing response was limited, these results thus suggest that the brain response observed after the startle stimulus is likely to come from the movement rather than the startle itself, as shown in Figs. 3 and 4.

These results benefit of the simultaneous study of extra-cerebral and cerebral tissue layers that helped to identify a classical neuroactivation when occurring.

The neuroimaging data on sheep obtained in this study (see Supplementary Section S1) indicated that in our experimental setting the fNIRS sensors were placed above the motor cortex of the sheep and recorded the vascular dynamics related to Brodmann area 4 (for extended discussion and references on the position and connections of the motor cortex of the sheep see Ref.⁴²). Overall, the results of the startling test and of the motor task furtherly indicate that we are mainly measuring the motor area of the sheep brain, and that we are not probing the too deeply located “prefrontal” cortex of the supraorbital gyrus or other cortical areas related to processing of emotions. In fact, DTI MRI data also confirm that the fiber tracts that originate from the cortical area under the fNIRS probe belong to the pyramidal and extrapyramidal motor control pathways that project to the generators of motor schemes in the brainstem or to the spinal cord, either homolaterally or (mostly) contralaterally⁴²).

The positioning of the fNIRS probe, constrained by the dimensions of the animals' heads, and the basic characteristics of the fNIRS device (e.g. wavelength range, optical power) were similar to previous published work^{23,26–28}. Differently from other studies, thanks to the use of proper short distance and long distance channels, we were able to clearly discriminate the contributions from extra-cerebral and cerebral tissue. Our experience suggests that inconsistent and conflicting fNIRS results on the emotional and cognitive responses of animals reported in literature^{6,30} can be explained by the fact that it is very unlikely that the photons may reach the sheep equivalent of the human pre-frontal cortex and other areas dedicated to processing of cognitive stimuli, placed too distant from scalp, and the respiratory sinuses immediately below it in the animal calvaria (see Supplementary Section S1 and Supplementary Section S3).

Although we carefully evaluated all the potential confounding factors of previous experimental works, we are also aware that there are still some limitations that could affect the outcome of this research.

The choice of the location of the fNIRS probe was determined by the anatomical configuration of the head of the sheep. The natural curvature of the skull allowed positioning the sensors only on the top part of the head and prevented the use of larger source detector distances ($\rho > 30$ mm). Further, a shorter source detector distance ($\rho < 10$ mm) could be beneficial to better discriminating extra-cerebral and intra cerebral layers, but it was prevented in our work by the specific configuration of the fNIRS sensors.

We only had a limited number of fNIRS sensors that prevented mapping the hemodynamic response with a better lateral resolution, e.g. differentiating anterior and posterior parts of cerebral cortex. Mapping is important if one is interested in understanding the specific mechanism and *all* the different cortical areas involved in

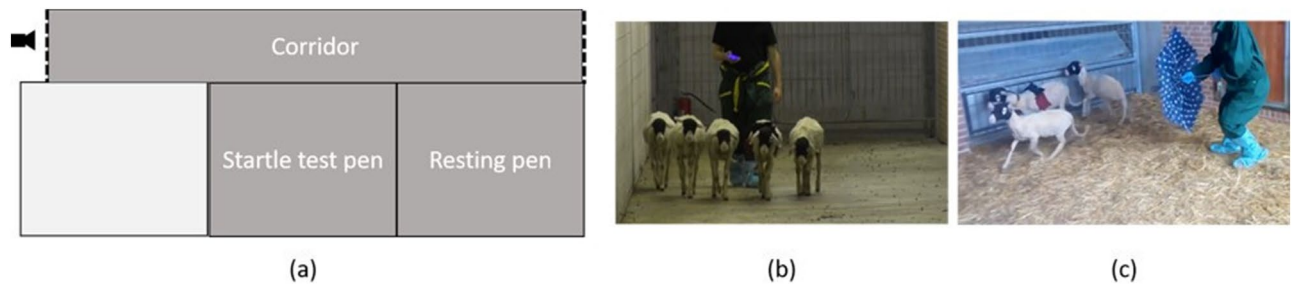


Figure 5. Schematic representation of the experimental area (a), the dotted lines represent mobile fences, the white line represents a wood door between the two pens; corridor (b) and startling test pen (c).

execution of the movement. Movement is in fact a complex task involving multiple regions of the brain⁴³; for a review of the organization of the motor cortex in large herbivores and extended references see Ref.⁴⁴. Therefore, in our work when the sheep were moving, the specific working mechanism in the brain and the response of multiple brain areas could not be studied in detail and need to be further investigated.

We have measured the baseline optical properties of the head of the sheep by using a homogeneous model. The time-resolved diffuse spectroscopy system that we used had a limited responsivity that prevented acquiring multi-distance measurements at several discrete wavelengths (needed for proper application of a two-layer model) within an overall acquisition time sufficiently short not to induce stress in the measured animal. Refining the estimate of baseline optical properties could further improve the quantification of the hemodynamic response.

Similarly, assuming that the reduced scattering coefficient is constant in time (during the experiments) and space (in extra- and intra-cerebral body layers) could affect the accuracy of the hemodynamic response. However, it is unlikely that the reduced scattering coefficient varies appreciably during functional tests.

We have disregarded the contribution of other chromophores (e.g. water, lipid, collagen) in the estimate of the concentration of (baseline and transient) O₂Hb and HHb. Like for the reduced scattering coefficient we do not expect these parameters to vary significantly during the functional tests.

In the pre-processing phase, the removal of blocks was based on the visual inspection of the video recordings. Another more objective method for artifacts removal, especially motion artifacts, is the use of accelerometers²⁵. Since the used fNIRS device was not equipped with a built sensor for acceleration we have preferred not to complicate further the experimental setup by adding another sensor on the limited space on the head of the animal.

Finally, the current work does not give a definitive conclusion about the brain response pattern of sheep undergoing behavioral tasks. A clear and definite brain response pattern is actually difficult to obtain from one or few experiments, which require repeated trials or a larger animal sample. The fNIRS technique represents still an innovative approach for studying cortex activity in freely moving animals and the number of studies performed using fNIRS on animals is still low.

Methods

Ethical statement. All methods on animals were carried out in accordance with relevant guidelines and regulations, and all experimental protocols were approved by a named institutional and/or licensing committee. In particular, the study design, which was created in compliance with Italian legislation on animal experiments, was approved by the national ethical commission (Ministero della Salute, Direzione Generale della Sanità Animale e dei Farmaci Veterinari, Ufficio 6, authorization n°457/2016-PR, 919/2017-PR). If any animal was deemed to be in greater than mild stress (assessed live by an independent veterinarian), then it would immediately be removed from the study.

Animals, housing and husbandry. Thirteen 8-month-old Sarda sheep were selected from the same flock. All sheep were no gestating nor lactating and they had never been involved in any study before. They were group housed in a 45 m² pen (resting box), fed with hay twice a day (8 a.m. and 6 p.m.). Diet was supplemented with a commercial concentrate (Mangimi Ariston Srl, Teramo, Italy; 250–300 g/sheep). All sheep had free access to water and straw was provided for bedding.

Experimental area and behavioral tasks. To measure the cerebral activity in different conditions, all sheep underwent to a motor task and a startling test. The experimental area (Fig. 5) was familiar to the sheep and it comprised a corridor (2 m wide × 20 m long) and a startle test pen. The end of the corridor was closed with metal panels routinely used for building animal enclosures (height 1.5 m). The startle test pen was similar to the pen where the sheep were housed. To avoid any negative impact of being isolated from the flock during behavioral tasks, sheep were always kept in small groups (3–5 subjects).

The motor task consisted in sheep walking at the same speed along the corridor and stop when asked. Therefore, five sheep at each time were moved in the corridor and trained to walk slowly and calmly for 30 s and stop for the following 30 s. For this reason, they were trained through classical conditioning to start and stop walking on a vocal cue. The training was performed every day, for 26 days. We gradually habituated the sheep to wear a fake fNIRS probe, including cap, cables and chest straps, following the scheme: days 1–7 sheep were walking without any probe; days 8–14 sheep were walking wearing the supporting masks for the probe; days 15–26 sheep

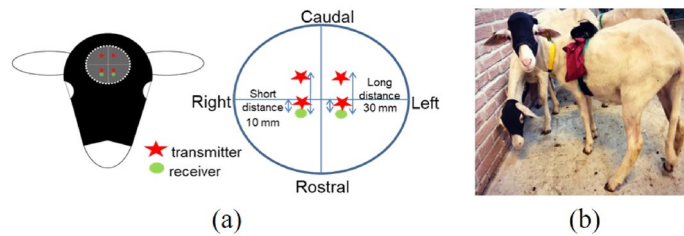


Figure 6. (a) The configuration of optical probes on the surface of sheep head: red stars represent the transmitters and green circles represent the receivers. (b) Sheep equipped with fNIRS devices.

were walking with wearing the supporting masks for the probe and a sponge mimicking the probe pressure. At the end of the training phase no sign of stress was shown by the sheep.

The startling test consisted in an umbrella suddenly opened near the animals, able to evoke a fear reaction. To reduce the impact of habituation to the startling stimulus, sheep selected for fNIRS measurement were never been exposed to this stimulus before.

fNIRS data recording and data analysis. To accurately measure concentration changes in oxygenated hemoglobin ($[\Delta O_2Hb]$) and deoxygenated hemoglobin ($[\Delta HHb]$) in each sheep undergoing different behavioral tasks, a wearable CW-fNIRS system (OctaMon, Artinis Medical Systems, The Netherlands) operating at a sampling rate of 10 Hz, at two wavelengths (751 nm and 839 nm), and equipped with 4 transmitters (light sources) and 2 receivers (detectors) was used. The device was customized by the manufacturer to enable multi-distance acquisition. Two light sources and one detector were placed on each hemisphere at a source detector distance $\rho = 10$ mm and $\rho = 30$ mm, respectively, as shown in Fig. 6a. This configuration allowed recording of signals from both superficial tissues (e.g. the scalp and skull) and from the cortical tissue. During fNIRS recording, the sensors were applied on the shaved sheep head and held in place with a customized head cap as shown in Fig. 6b.

The fNIRS recordings were completed in two consecutive days (first day motor task, second day startling test) for all sheep. In the motor task, for each sheep, we recorded 10 repetitions (blocks) each with 30 s of walking followed by 30 s of rest (animal stand still). For the startling test, for each sheep, we recorded 5 blocks consisting of a 30 s baseline (sheep stand still), followed by the umbrella opening (3 s) and then 60 s of fear reaction. All the blocks of both motor task and startling test were filmed with a video-camera (Panasonic, HDC-SD99, Panasonic, Japan) and synchronized with fNIRS recordings. Video recordings were then analyzed using the software Solomon Coder (version beta 11.01. 22) to identify whether the sheep showed behaviors that could interfere with fNIRS recording such as head shaking, running and jumping. For the startle test, fear reaction (presence of flight and/or freezing response after the stimulus) was evaluated. The ethogram of behaviors considered is presented in the Supplementary Table ST2.

The fNIRS data were analyzed by a script in Matlab2015a (Matlab, The MathWorks Inc., Natick, Massachusetts). The raw fNIRS data extracted by the software Oxysoft (v3.0.95, Artinis Medical Systems, The Netherlands) were the optical density (OD) for each wavelength and each channel. For each task the last 5 s before each block were chosen as baseline. The change in OD relative to the baseline (i.e. ΔOD) were then calculated by subtracting the average OD of the baseline periods from all OD values.

According to anatomical and MRI measurements of sheep of the same age, the average distance between scalp and brain cortex was estimated to be $s = 10$ mm. Given this, we assumed (see Supplementary Section S3) that the ΔOD data from $\rho = 10$ mm (ΔOD_{SHORT}) referred to photons that travelled exclusively in the extra-cerebral tissue (scalp, skull, and CSF). Therefore, using a Levenberg–Marquardt algorithm for nonlinear iterative least squares minimization (lsqcurvefit function in Matlab), and assuming the reduced scattering coefficient of the upper layer (representing extra-cerebral tissue) equal to the baseline value ($\mu_s^{UP} = \mu_{s0}^{UP}$), we fitted ΔOD_{SHORT} data to a homogenous model⁴⁵ to estimate the absorption changes relative to the baseline in the upper layer ($\Delta\mu_a^{UP}$). The absolute value of the absorption coefficient in the upper layer was then calculated as $\mu_a^{UP} = \mu_{a0} + \Delta\mu_a^{UP}$, by adding to $\Delta\mu_a^{UP}$ the baseline absorption coefficient μ_{a0} (see Supplementary Section S2 for description of μ_{a0} estimate).

Next we used ΔOD recorded at $\rho = 30$ mm (ΔOD_{LONG}) and a two-layer model for photon migration⁴⁶, to derive $\Delta\mu_a^{DOWN}$, i.e. the change in the absorption coefficient in the bottom layer (representing cerebral tissue). In this step we assumed as a priori information the thickness of the upper layer ($s = 10$ mm), the absorption coefficient of the upper layer (μ_a^{UP}) and the reduced scattering coefficient of the upper and bottom layer ($\mu_s^{UP} = \mu_s^{DOWN} = \mu_{s0}^{UP}$). The absolute value of the absorption coefficient in the bottom layer was then calculated as $\mu_a^{DOWN} = \mu_{a0} + \Delta\mu_a^{DOWN}$.

Finally, from μ_a^{UP} and μ_a^{DOWN} at the two wavelengths, $[O_2Hb]$ and $[HHb]$ in both layers were calculated by the Beer's law using the extinction coefficients derived from the measurement of adult sheep⁴⁷ for $[HHb]$: $1.672 \text{ cm}^{-1} \text{ mM}^{-1}$ (751 nm), $0.824 \text{ cm}^{-1} \text{ mM}^{-1}$ (839 nm), and for $[O_2Hb]$: $0.752 \text{ cm}^{-1} \text{ mM}^{-1}$ (751 nm), $1.084 \text{ cm}^{-1} \text{ mM}^{-1}$ (839 nm).

Conclusion

Our goal in this study was to improve fNIRS measurement accuracy and reliability in sheep to better understand the potential to noninvasively assess the cerebral activity of freely moving animals under different environmental conditions. Our findings confirmed that multi-distance CW-fNIRS allowed to noninvasively measure cerebral

cortex activity in freely moving sheep and that the use of short and long-distance pairs of source-detector, coupled to a two-layer model for photon diffusion, can effectively discriminate extra-cerebral signals from cortical signals. Overall, these results indicate that with the current setup and probe placement we are primarily measuring the motor area of the sheep brain. Further investigations are needed to clarify whether fNIRS technique can be reliably applied to measure the deeply located cortical areas involved in processing affective state reactions. Future work must also consider possible factors that affect the accurateness of measurement such as probe location, and the species-specific neuroanatomical location corresponding to cognitive function.

Received: 24 February 2020; Accepted: 7 August 2020

Published online: 07 September 2020

References

1. John, S. E. *et al.* The ovine motor cortex: a review of functional mapping and cytoarchitecture. *Neurosci. Biobehav. Rev.* **80**, 306–315 (2017).
2. Kendrick, K. M., Atkins, K., Hinton, M. R., Heavens, P. & Keverne, B. Are faces special for sheep? Evidence from facial and object discrimination learning tests showing effects of inversion and social familiarity. *Behav. Processes* **38**, 19–35 (1996).
3. Boissy, A. *et al.* Cognitive sciences to relate ear postures to emotions in sheep. *Anim. Welf.* **20**, 47–56 (2011).
4. Kendrick, K. M., Da Costa, A. P., Leigh, A. E., Hinton, M. R. & Peirce, J. W. Sheep don't forget a face. *Nature* **414**, 165–166 (2001).
5. Peruffo, A. & Cozzi, B. Bovine brain: an in vitro translational model in developmental neuroscience and neurodegenerative research. *Front. Pediatr.* **2**, 10–13 (2014).
6. Kim, H. Y., Seo, K., Jeon, H. J., Lee, U. & Lee, H. Application of functional near-infrared spectroscopy to the study of brain function in humans and animal models. *Mol. Cells* **40**, 523–532 (2017).
7. Goense, J. B. M. & Logothetis, N. K. Neurophysiology of the BOLD fMRI signal in awake Monkeys. *Curr. Biol.* **18**, 631–640 (2008).
8. Berns, G. S., Brooks, A. M. & Spivak, M. Functional MRI in awake unrestrained dogs. *PLoS ONE* **7**, e38027 (2012).
9. Min, H. K. *et al.* Deep brain stimulation induces BOLD activation in motor and non-motor networks: an fMRI comparison study of STN and EN/GPi DBS in large animals. *Neuroimage* **63**, 1408–1420 (2012).
10. Lee, W. *et al.* Functional and diffusion tensor magnetic resonance imaging of the sheep brain. *BMC Vet. Res.* **11**, 1–8 (2015).
11. Cook, P. F., Brooks, A., Spivak, M. & Berns, G. S. Regional brain activations in awake unrestrained dogs. *J. Vet. Behav. Clin. Appl. Res.* **16**, 104–112 (2016).
12. Thompkins, A. M., Deshpande, G., Waggoner, P. & Katz, J. S. Functional magnetic resonance imaging of the domestic dog: research, methodology, and conceptual issues. *Comp. Cogn. Behav. Rev.* **11**, 63–82 (2016).
13. Berns, G. S., Brooks, A. M., Spivak, M. & Levy, K. Functional MRI in awake dogs predicts suitability for assistance work. *Sci. Rep.* **7**, 1–10 (2017).
14. Huber, L. & Lamm, C. Understanding dog cognition by functional magnetic resonance imaging. *Learn Behav* **45**, 101–102 (2017).
15. Ong, R. M. *et al.* Behavioural and EEG changes in sheep in response to painful acute electrical stimuli. *Aust. Vet. J.* **75**, 189–193 (1997).
16. Steiss, J. E. A survey of current techniques in veterinary electrodiagnostics: EEG, spinal evoked and brainstem auditory evoked potential recording. *Vet. Res. Commun.* **12**, 281–288 (1988).
17. Cwynar, P. & Zawadzka, W. Recording of bioelectrical activity changes in sheep cerebral cortex. *Arch. Med. Vet.* **42**, 51–62 (2010).
18. Drinkenburg, W. H. I. M., Ahnaou, A. & Ruigt, G. S. F. Pharmacology-EEG studies in animals: a history-based introduction to contemporary translational applications. *Neuropsychobiology* **72**, 139–150 (2016).
19. Williams, D. C. *et al.* Electroencephalogram of healthy horses during inhaled Anesthesia. *J. Vet. Intern. Med.* **30**, 304–308 (2016).
20. Villringer, A. & Chance, B. Non-invasive optical spectroscopy and imaging of human brain function. *Trends Neurosci.* **20**, 435–442 (1997).
21. Scholkmann, F. *et al.* A review on continuous wave functional near-infrared spectroscopy and imaging instrumentation and methodology. *Neuroimage* **85**, 6–27 (2014).
22. Boas, D. A., Elwell, C. E., Ferrari, M. & Taga, G. Twenty years of functional near-infrared spectroscopy: introduction for the special issue. *Neuroimage* **85**, 1–5 (2014).
23. Gygas, L., Reefmann, N., Wolf, M. & Langbein, J. Prefrontal cortex activity, sympatho-vagal reaction and behaviour distinguish between situations of feed reward and frustration in dwarf goats. *Behav. Brain Res.* **239**, 104–114 (2013).
24. Gygas, L., Reefmann, N., Pilheden, T., Scholkmann, F. & Keeling, L. Dog behavior but not frontal brain reaction changes in repeated positive interactions with a human: a non-invasive pilot study using functional near-infrared spectroscopy (fNIRS). *Behav. Brain Res.* **281**, 172–176 (2015).
25. Muehleemann, T., Reefmann, N., Wechsler, B., Wolf, M. & Gygas, L. In vivo functional near-infrared spectroscopy measures mood-modulated cerebral responses to a positive emotional stimulus in sheep. *Neuroimage* **54**, 1625–1633 (2011).
26. Vögeli, S., Lutz, J., Wolf, M., Wechsler, B. & Gygas, L. Valence of physical stimuli, not housing conditions, affects behaviour and frontal cortical brain activity in sheep. *Behav. Brain Res.* **267**, 144–155 (2014).
27. Vögeli, S., Wolf, M., Wechsler, B. & Gygas, L. Frontal brain activity and behavioral indicators of affective states are weakly affected by thermal stimuli in sheep living in different housing conditions. *Front. Vet. Sci.* **2**, 1–10 (2015).
28. Guldemann, K., Vögeli, S., Wolf, M., Wechsler, B. & Gygas, L. Frontal brain deactivation during a non-verbal cognitive judgement bias test in sheep. *Brain Cogn.* **93**, 35–41 (2015).
29. Chincarini, M. *et al.* Evaluation of sheep anticipatory response to a food reward by means of functional near-infrared spectroscopy. *Animals* **9**, 1–13 (2019).
30. Gygas, L. & Vögeli, S. Reactions of sheep towards three sets of emotional stimuli: (in)consistency in respect to stimulus valence and sheep identity. *Appl. Anim. Behav. Sci.* **174**, 51–57 (2016).
31. Muehleemann, T., Haensse, D. & Wolf, M. Wireless miniaturized in-vivo near infrared imaging. *Opt. Express* **16**, 10323 (2008).
32. Nitzsche, B. *et al.* A stereotaxic, population-averaged T1w ovine brain atlas including cerebral morphology and tissue volumes. *Front. Neuroanat.* **9**, 1–14 (2015).
33. Aasted, C. M. *et al.* Anatomical guidance for functional near-infrared spectroscopy: atlas viewer tutorial. *Neurophotonics* **2**, 020801 (2015).
34. Li, L., Cazzell, M., Babawale, O. & Liu, H. Automated voxel classification used with atlas-guided diffuse optical tomography for assessment of functional brain networks in young and older adults. *Neurophotonics* **3**, 045002 (2016).
35. Clancy, M. *et al.* Improving the quantitative accuracy of cerebral oxygen saturation in monitoring the injured brain using atlas based near infrared spectroscopy models. *J. Biophotonics* **9**, 812–826 (2016).
36. Pringle, J., Roberts, C., Kohl, M. & Lekeux, P. Near infrared spectroscopy in large animals: optical pathlength and influence of hair covering and epidermal pigmentation. *Vet. J.* **158**, 48–52 (1999).

37. Sanna, S. R., Carta, A. & Casu, S. Genotype by environment interaction for milk yield in Sarda dairy sheep. *J. Anim. Breed. Genet.* **119**, 190–199 (2002).
38. Santos, B. F. S., Van Der Werf, J. H. J., Gibson, J. P., Byrne, T. J. & Amer, P. R. Genetic and economic benefits of selection based on performance recording and genotyping in lower tiers of multi-tiered sheep breeding schemes. *Genet. Sel. Evol.* **49**, 1–16 (2017).
39. Cannas, S. *et al.* Thermography as a non-invasive measure of stress and fear of humans in sheep. *Animals* **8**, 146 (2018).
40. Boas, D. A., Strangman, G., Culver, J. P., Hoge, R. D. & Jaszewski, G. Can the cerebral metabolic rate of oxygen be estimated with near-infrared spectroscopy? *Phys. Med. Biol.* **48**, 2405–2418 (2003).
41. Vitorio, R., Stuart, S., Rochester, L., Alcock, L. & Pantall, A. fNIRS response during walking—artefact or cortical activity? A systematic review. *Neurosci. Biobehav. Rev.* **83**, 160–172 (2017).
42. Peruffo, A. *et al.* The motor cortex of the sheep: laminar organization, projections and diffusion tensor imaging of the intracranial pyramidal and extrapyramidal tracts. *Brain Struct. Funct.* **224**, 1933–1946 (2019).
43. Newton, C. D. & Fletcher, T. F. Effect of motor cortex ablation on conditioned learning in sheep. *Am. J. Vet. Res.* **30**, 1765–1772 (1969).
44. Cozzi, B. *et al.* The laminar organization of the motor cortex in monodactylous mammals: a comparative assessment based on horse, chimpanzee, and macaque. *Brain Struct. Funct.* **222**, 2743–2757 (2017).
45. Contini, D., Martelli, F. & Zaccanti, G. Photon migration through a turbid slab described by a model based on diffusion approximation. I. Theory. *Appl. Opt.* **36**, 4587–4599 (1997).
46. Liemert, A. & Kienle, A. Light diffusion in N-layered turbid media: steady-state domain. *J. Biomed. Opt.* **15**, 025003 (2010).
47. Zijlstra, W. G., Buursma, A. & Van Assendelft, O. W. *Visible and Near Infrared Absorption Spectra of Human and Animal Haemoglobin determination and application* (CRC Press, Boca Raton, 2000).
48. Martinenghi, E. *et al.* Time-resolved single-photon detection module based on silicon photomultiplier: a novel building block for time-correlated measurement systems. *Rev. Sci. Instrum.* **87**, 073101 (2016).
49. Cubeddu, R., Pifferi, A., Taroni, P., Torricelli, A. & Valentini, G. Experimental test of theoretical models for time-resolved reflectance. *Med. Phys.* **23**, 1625–1633 (1996).
50. Delpy, D. T. *et al.* Estimation of optical pathlength through tissue from direct time of flight measurement. *Phys. Med. Biol.* **33**, 1433–1442 (1988).
51. Wyatt, J. S. *et al.* Measurement of optical path length for cerebral near-infrared spectroscopy in newborn infants. *Dev. Neurosci.* **12**, 140–144 (1990).
52. Scholkman, F. & Wolf, M. General equation for the differential pathlength factor of the frontal human head depending on wavelength and age. *J. Biomed. Opt.* **18**, 105004 (2013).
53. Mourant, J. R., Fuselier, T., Boyer, J., Johnson, T. M. & Bigio, I. J. Predictions and measurements of scattering and absorption over broad wavelength ranges in tissue phantoms. *Appl. Opt.* **36**, 949–957 (1997).
54. Caldwell, M. *et al.* Modelling confounding effects from extracerebral contamination and systemic factors on functional near-infrared spectroscopy. *Neuroimage* **143**, 91–105 (2016).
55. Martelli, F. *et al.* There's plenty of light at the bottom: statistics of photon penetration depth in random media. *Sci. Rep.* **6**, 27057 (2016).
56. Okamoto, M. *et al.* Three-dimensional probabilistic anatomical cranio-cerebral correlation via the international 10–20 system oriented for transcranial functional brain mapping. *Neuroimage* **21**, 99–111 (2004).
57. Brigadoi, S. & Cooper, R. J. How short is short? Optimum source–detector distance for short-separation channels in functional near-infrared spectroscopy. *Neurophotonics* **2**, 025005 (2015).
58. Carraresi, S., Shatir, T. S. M., Martelli, F. & Zaccanti, G. Accuracy of a perturbation model to predict the effect of scattering and absorbing inhomogeneities on photon migration. *Appl. Opt.* **40**, 4622–4632 (2001).
59. Schindelin, J. *et al.* Fiji—An open source platform for biological image analysis. *Nat. Methods* **28**, 676–682 (2012).
60. Fang, Q. & Boas, D. A. Tetrahedral mesh generation from volumetric binary and gray-scale images. In *Proceedings of the 6th IEEE International Conference on Symposium on Biomedical Imaging: From Nano to Macro*, 1142–1145 (IEEE Press, 2009).
61. Fang, Q. Mesh-based Monte Carlo method using fast ray-tracing in Plücker coordinates. *Biomed. Opt. Express* **1**, 165 (2010).
62. Saager, R. B. & Berger, A. J. Direct characterization and removal of interfering absorption trends in two-layer turbid media. *J. Opt. Soc. Am. A Opt. image Sci. Vis.* **22**, 1874–1882 (2005).
63. Saager, R. & Berger, A. Measurement of layer-like hemodynamic trends in scalp and cortex: implications for physiological baseline suppression in functional near-infrared spectroscopy. *J. Biomed. Opt.* **13**, 034017 (2008).
64. Saager, R. B., Telleri, N. L. & Berger, A. J. Two-detector Corrected Near Infrared Spectroscopy (C-NIRS) detects hemodynamic activation responses more robustly than single-detector NIRS. *Neuroimage* **55**, 1679–1685 (2011).
65. Goodwin, J. R., Gaudet, C. R. & Berger, A. J. Short-channel functional near-infrared spectroscopy regressions improve when source-detector separation is reduced. *Neurophotonics* **1**, 015002 (2014).
66. Yücel, M. A. *et al.* Short separation regression improves statistical significance and better localizes the hemodynamic response obtained by near-infrared spectroscopy for tasks with differing autonomic responses. *Neurophotonics* **2**, 035005 (2015).
67. Bhutta, M. R. *et al.* Note: Three wavelengths near-infrared spectroscopy system for compensating the light absorbance by water. *Rev. Sci. Instrum.* **85**, 026111 (2014).
68. Umeyama, S. & Yamada, T. Monte Carlo study of global interference cancellation by multidistance measurement of near-infrared spectroscopy. *J. Biomed. Opt.* **14**, 064025 (2009).
69. Eggebrecht, A. T. *et al.* Mapping distributed brain function and networks with diffuse optical tomography. *Nat. Photonics* **8**, 448–454 (2014).
70. Bonomini, V. *et al.* Linear regression models and k-means clustering for statistical analysis of fNIRS data. *Biomed. Opt. Express* **6**, 615–630 (2015).

Acknowledgements

Thanks to Luca Bonfanti (Dept. of Veterinary Sciences, University of Turin, Neuroscience Institute Cavalieri Ottolenghi—NICO) for the useful insights and cooperation in the design of the experimental protocol. Thanks to Enrico Grisan (Dept. of Information Engineering of the University of Padova, Italy) for analyses and elaboration of DTI data. Thanks to Alwin Kienle and André Liemert (Institut für Lasertechnologien in der Medizin und Meßtechnik an der Universität Ulm, Germany) for providing the Matlab script of the reflectance in a two-layer diffusive medium. This work was partially supported by MIUR-PRIN2015 (Grant Number 2015Y5W9YP). Daniele Ancora acknowledges funding from the European Union's Horizon 2020 research and innovation programme under the Marie Skłodowska-Curie Grant Agreement No. 799230 (H2020-MSCA-IF-2017, Project Acronym: HI-PHRET).

Author contributions

M.C., G.V., N.F. were responsible for animal housing and husbandry. L.Q., L.S., A.T. were responsible for the fNIRS data recording and analysis. L.Q., D.A., L.S., A.T. were responsible for fNIRS numerical simulations. M.C., G.V., F.D.P., B.C. were responsible for MRI and DTI data recording and analysis. E.D.C., S.C., C.P., E.C., M.M. were responsible for animal behavioral data recording and analysis. M.C., G.V., E.D.C., C.P., E.C., M.M., B.C., L.S., A.T. conceived the experiments. M.C., G.V., E.D.C., C.P., M.M., L.Q., L.S., A.T. conducted the experiments. M.C., E.D.C., L.Q. wrote the draft manuscript. ALL authors reviewed the manuscript.

Competing interests

The authors declare no competing interests.

Additional information

Supplementary information is available for this paper at <https://doi.org/10.1038/s41598-020-71704-5>.

Correspondence and requests for materials should be addressed to A.T.

Reprints and permissions information is available at www.nature.com/reprints.

Publisher's note Springer Nature remains neutral with regard to jurisdictional claims in published maps and institutional affiliations.



Open Access This article is licensed under a Creative Commons Attribution 4.0 International License, which permits use, sharing, adaptation, distribution and reproduction in any medium or format, as long as you give appropriate credit to the original author(s) and the source, provide a link to the Creative Commons licence, and indicate if changes were made. The images or other third party material in this article are included in the article's Creative Commons licence, unless indicated otherwise in a credit line to the material. If material is not included in the article's Creative Commons licence and your intended use is not permitted by statutory regulation or exceeds the permitted use, you will need to obtain permission directly from the copyright holder. To view a copy of this licence, visit <http://creativecommons.org/licenses/by/4.0/>.

© The Author(s) 2020

Supplementary data

Title:

Reliability of fNIRS for noninvasive monitoring of brain function and emotion in sheep

Authors:

Matteo Chincaroni^{1*}, Emanuela Dalla Costa^{2*}, Lina Qiu^{3,4*}, Lorenzo Spinelli⁵, Simona Cannas², Clara Palestrini², Elisabetta Canali², Michela Minero², Bruno Cozzi⁶, Nicola Ferri⁷, Daniele Ancora³, Francesco De Pasquale¹, Giorgio Vignola¹, and Alessandro Torricelli^{3,5}

Affiliations:

- 1 Università degli Studi di Teramo, Facoltà di Medicina Veterinaria, Teramo (Italy)
- 2 Università degli Studi di Milano, Dipartimento di Medicina Veterinaria, Milan (Italy)
- 3 Politecnico di Milano, Dipartimento di Fisica, Milan (Italy)
- 4 School of Software, South China Normal University, Guangzhou (China)
- 5 Istituto di Fotonica e Nanotecnologie, Consiglio Nazionale delle Ricerche, Milan (Italy)
- 6 Università degli Studi di Padova, Dipartimento di Biomedicina Comparata e Alimentazione, Padova (Italy)
- 7 Istituto Zooprofilattico Sperimentale dell'Abruzzo e del Molise G. Caporale, Teramo (Italy)

Corresponding authors:

mchincaroni@unite.it, emanuela.dallacosta@unimi.it, alessandro.torricelli@polimi.it

* Equally contributed to the manuscript

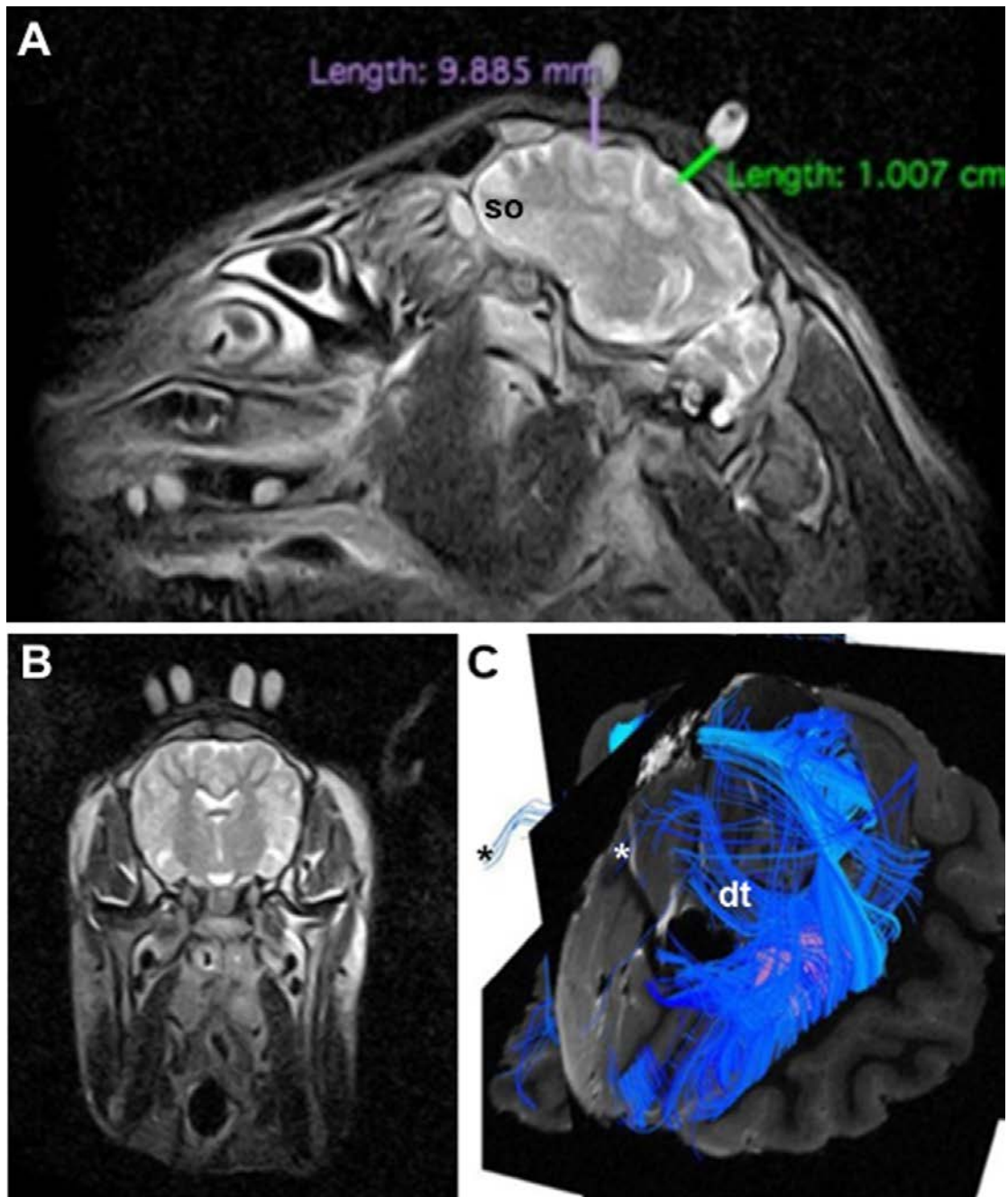
Supplementary Section S1 Neuro-anatomical imaging of the sheep's head

We guided the positioning of the fNIRS probe by MRI data of the very same animals, and checked the functional origin of the signal by diffusion tensor imaging (DTI) MRI on the animal brain.

Preliminary MR scans were used to obtain relative position of the brain within the surrounding structures of the head. The MR data were acquired by means of an ESAOTE VETSCAN MR-Grande operating at 0.25 T. T1 weighted images were obtained with 2D Spin Echo T1 sequences with the following parameters: Slice Thickness = 3 mm, Repetition Time TR = 980 ms, EchoTime TE = 18 ms, Number of Averages: 2, Field of View FOV = 230x230 mm². A total of 27 slices were acquired. T2 weighted images were acquired through a 2D Fast Spin Echo T2 sequence with the following parameters: Slice Thickness: 3 mm, Repetition Time TR = 6030 mm, Echo Time TE = 100 ms, Number of Averages: 2, Field of View = 230x230 mm². A total of 27 slices were acquired.

For DTI we utilized the brains of six adult sheep, whose heads were collected at a commercial abattoir during routine slaughtering procedures. Slaughtering was performed according to the European Community Council directive (86/609/EEC) that regulates animal welfare during the whole commercial process and guarantees that animals are treated humanely and constantly monitored under mandatory official veterinary medical care. Once removed from the head, the brains were immediately fixed by immersion in cold buffered formalin. The time interval between death and removal of the brain varied between 10 and 20 minutes. The fixed brains were subsequently transported to the Department of Computer Science of the University of Verona for MR scans, using a 4.7 Tesla (T) magnet. Images were acquired with an Echo Planar Imaging (EPI) sequence with the following parameters: TR 20000 ms, TE 24.7 ms, FOV = 6.0x5.0 cm²; MTX 120x100; isotropic in-plane resolution of 0.500 mm; slice thickness 1.0 mm; number of slice 80; EPI factor 11; NEX 6; 30 non-collinear directions acquired with a b-value of 3000 s/mm² and 5 b₀ images for a total acquisition time of about 12 h 50 min (for further details and discussion of motor projections see Ref.⁴²).

From MRI and DTI data we confirmed that the location of the fNIRS probe was over the motor area of the cortex (see Supplementary Figure SF1).



Supplementary Figure SF1. Images from MR scans (panel A, sagittal view; panel B, coronal view) and DTI (panel C). (so: supraorbital gyrus; dt: descending motor tracts; *: location of motor cortex, Brodmann area 4).

Supplementary Section S2 Baseline optical properties and DPF of the sheep's head

A time domain diffuse spectroscopy system was used to estimate the baseline optical properties (absorption coefficient, μ_{a0} and reduced scattering coefficient, μ'_{s0}) and the DPF of the head of the sheep. A supercontinuum fiber laser (SC450-6W, Fianium, UK) and a set of interference filters (Hard Coated OD 4 10nm Bandpass Filters, Edmund Optics Ltd. UK) were used to sequentially produce laser pulses (duration <100 ps, repetition rate 37 MHz, average power < 2 mW) at 671, 730, 780, and 830 nm. Multimode graded index glass (core diameter 0.1 mm) and plastic (core diameter 1.0 mm) optical fibers were used to inject and collect light into the head of the sheep, respectively. A home-made solid-state large area SiPM detector (developed at the Department of Physics of Politecnico di Milano)⁴⁸ and a time-correlated single photon counting board (SPC130 Becker-Hickl GmbH, Germany) were used to acquire the photon distribution of time of flights (DTOF). Measurements were performed with a source detector distance $\rho = 25$ mm over the right and left hemisphere of nine sheep (2337, 2339, 2345, 2349, 3908, 3909, 3911, 3913, 3919) while they were standing still, gently blocked by two people. The acquisition time was 1 s for each wavelength, while <10 s were needed to change wavelength and optimize the collected signal. Three repetitions for each position were acquired, resulting overall in about 4 minutes for each sheep.

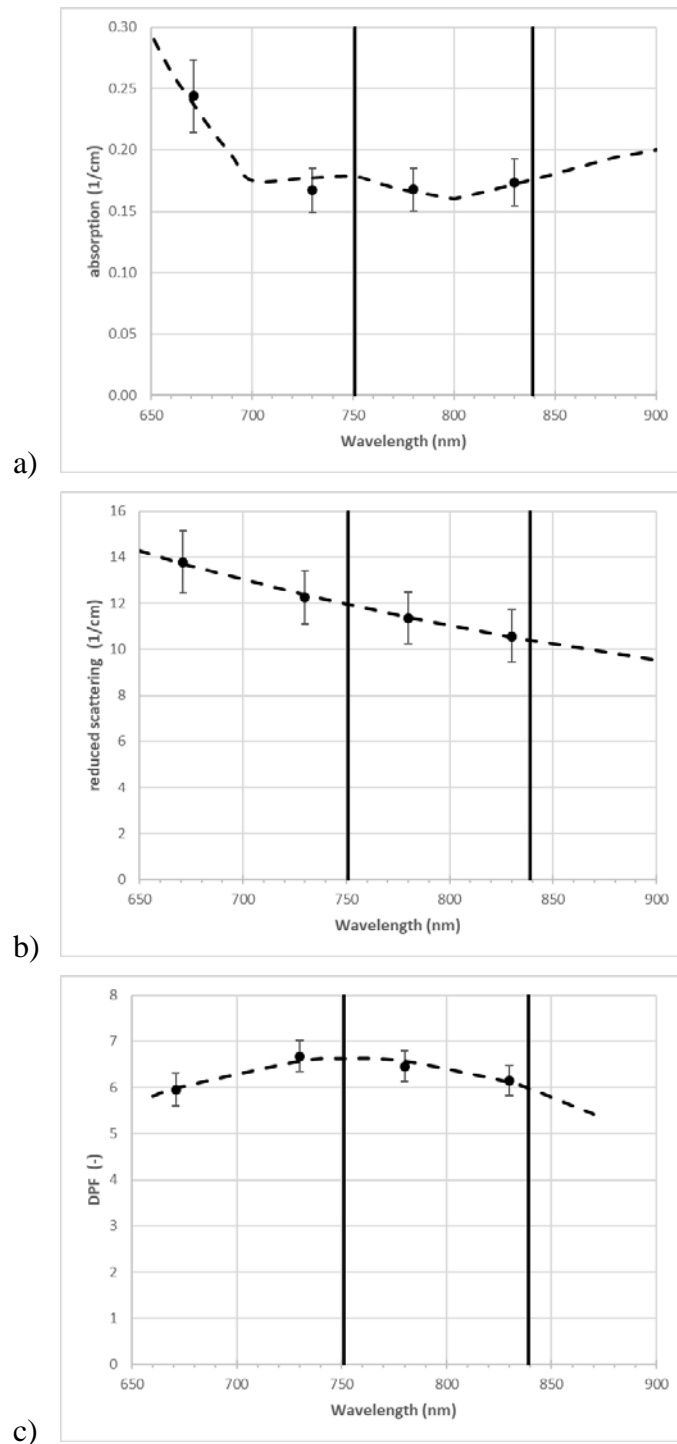
A physical model for time-resolved reflectance in a homogeneous medium⁴⁵ was used to fit the DTOF after convolution with the instrument response function⁴⁹. The fitting range was fixed at 90% and 1% of the peak on the leading and trailing edge of the DTOF. Values for μ_{a0} and μ'_{s0} were derived by averaging the results of the three repetitions in each hemisphere. From the DTOF we estimated the DPF as $DPF = v \langle t \rangle / \rho$, where $v = c/n$ is the speed of light, $n = 1.4$ is the refractive index, and $\langle t \rangle$ is the photon mean time-of-flight (i.e. the barycenter or first order moment of the DTOF)⁵⁰⁻⁵².

Supplementary Figure SF2 shows the average and standard deviation values for the baseline optical properties (panel a and b) and for the DPF (panel c) at 671, 730, 780, and 830 nm as obtained by the time domain diffuse spectroscopy data. The difference between left and right hemisphere is not significant, therefore for data analysis and for simulations we have averaged the data over all sheep and channels. To obtain the μ'_{s0} background values at 751 nm and 839 nm (the wavelengths used by the used CW fNIRS device) we have fitted the μ'_{s0} data at 671 nm, 730 nm, 780 nm and 830 nm with an empirical approximation to the Mie theory, $\mu'_{s0} = a(\lambda/\lambda_0)^{-b}$ where a and b are parameters related to density and size of scatterers and λ is the

wavelength⁵³. Similarly, we have fitted the μ_{a0} data at 671 nm, 730 nm, 780 nm and 830 nm to a linear combination of the contribution from HHb and O2Hb by means of the Beer's law (using the specific absorption of hemoglobin in sheep⁴⁷ and assuming a contribution from water 70%): average value for the absorption μ_{a0} are 0.178 cm^{-1} at 751 nm and 0.176 cm^{-1} at 839 nm, while the average values for the reduced scattering μ'_{s0} are 11.9 cm^{-1} at 751 nm and 10.4 cm^{-1} at 839 nm, as reported in in Supplementary Table ST1. We have also derived the values for the DPF at 739 nm and 851 nm by fitting the data at 671, 730, 780, and 830 nm to a quadratic polynomial function obtaining 6.6 and 6.0 at 751 nm and 839 nm, respectively.

Supplementary Table ST1. Average values and standard deviations of the head of the sheep for absorption coefficient, reduced scattering coefficient, and DPF at 671 nm, 730 nm, 780 nm, and 830 nm. Data at 739 nm and 851 nm are also shown as obtained from fitting of the μ_{s0}' data with an empirical approximation to the Mie theory⁵³, fitting the μ_{a0} data to Beer's law (using the specific absorption of hemoglobin in sheep⁴⁷, and fitting of DPF to a quadratic polynomial function.

	671 nm	730 nm	780 nm	830 nm	751 nm	839 nm
μ_{a0} (cm⁻¹)	0.244±0.029	0.167±0.018	0.168±0.017	0.174±0.019	0.178±0.018	0.176±0.019
μ_{s0}' (cm⁻¹)	13.8±1.4	12.3±1.2	11.4±1.1	10.6±1.1	11.9±1.2	10.4±1.1
DPF (-)	6.0±0.4	6.7±0.3	6.5±0.3	6.1±0.3	6.6±0.4	6.0±0.3



Supplementary Figure SF2. Average values and standard deviations of the head of the sheep for absorption coefficient (a), reduced scattering coefficient (b), and DPF (c) at 671 nm, 730 nm, 780 nm, and 830 nm. Data are averaged over three repetitions in the left and right hemisphere. Dashed lines represent fitting of absorption coefficient with Beer's law (a), fitting of reduced scattering coefficient with empirical approximation to Mie theory (b), fitting of DPF to a quadratic polynomial function (c). Vertical lines represent the wavelengths (751 nm and 839 nm) used by the CW fNIRS device.

Supplementary Section S3 Depth sensitivity

In fNIRS studies, task related and task unrelated physiological changes occurring in the scalp can introduce confounding signals often leading to false positives and artefacts⁵⁴. The adoption of a multi-distance approach is therefore essential in CW fNIRS to distinguish signals from shallow (e.g. scalp, skull and CSF) and deep (e.g. gray matter and white matter) layers in the head. This approach is justified by the physics of photon migration in diffusive media: in steady state (i.e. CW) the longer the source detector distance, the deeper is the average penetration depth⁵⁵. Given an average value of scalp to cortex distance of about 15 mm⁵⁶ in fNIRS studies on adult human subjects, channels with relatively short source detector distance (e.g. $\rho \leq 10$ mm) are typically only able to reach surface layers, while channels with relatively long separation (e.g. $\rho \geq 30$ mm) can typically reach deeper layers in the head such as gray matter⁵⁷.

It has been reported that the cerebral cortex of sheep is located about 5 to 9 mm below the scalp²⁵. According to anatomical and MRI measurements on the heads of several sheep of the same age (see Supplementary Section S1), for this study we could assume that the scalp and skull thickness of the sheep is on average 10 mm under the fNIRS probe. Therefore, in this study we used $\rho = 10$ mm and $\rho = 30$ mm as short and long channels, respectively. A shorter short distance (e.g. $\rho = 5$ mm) could not be used due to constraints in the shape of light emitter and detector of the CW fNIRS device we used. The use of a distance longer than 30 mm was prevented by the available space on the sheep head.

In order to have a rough estimate of the penetration depth of CW NIRS in our study, we calculated the mean maximum penetration depth ($\langle Z_{\max} | \rho \rangle$) of photons for a homogenous slab in CW domain based on the diffusion equation (see Eq. (24) in Ref.⁵⁵).

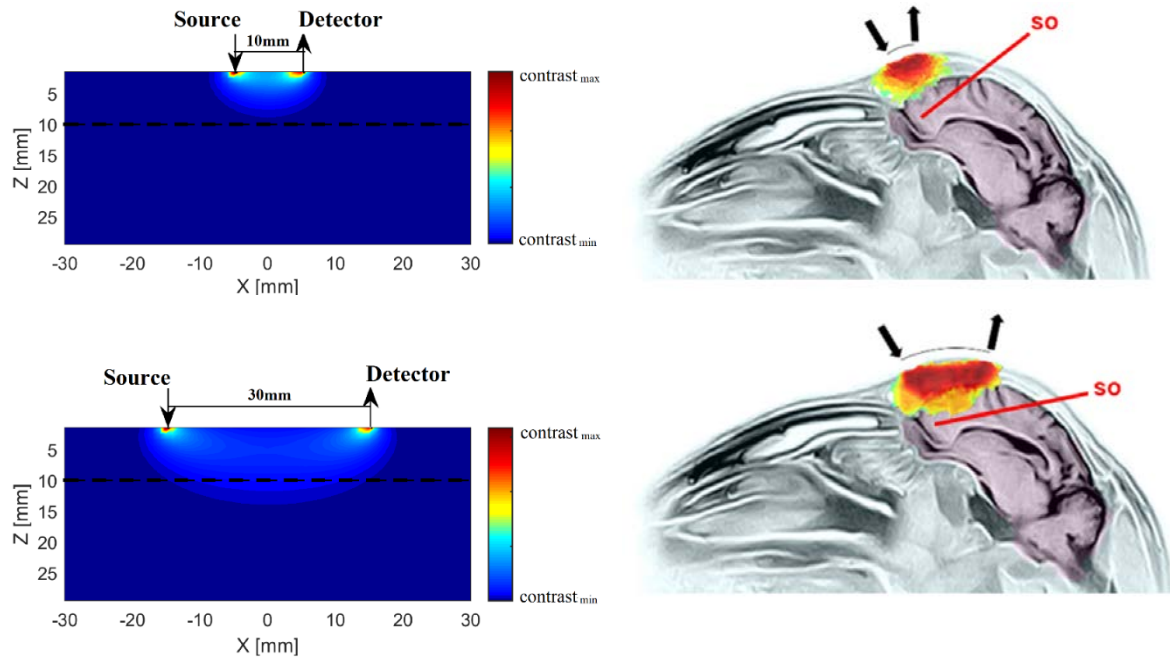
For a 30 mm thick homogenous slab with $\mu_a = 0.178$ cm⁻¹ and $\mu'_s = 11.9$ cm⁻¹, the mean maximum depths are $\langle Z_{\max} | \rho = 10$ mm $\rangle \approx 5.48$ mm and $\langle Z_{\max} | \rho = 30$ mm $\rangle \approx 11.60$ mm. While for the same slab with $\mu_a = 0.176$ cm⁻¹ and $\mu'_s = 10.4$ cm⁻¹, mean maximum depths are $\langle Z_{\max} | \rho = 10$ mm $\rangle \approx 5.53$ mm and $\langle Z_{\max} | \rho = 30$ mm $\rangle \approx 11.85$ mm.

To provide a representation of photon path in a diffusive two-layer medium we calculated the sensitivity maps for $\rho = 10$ mm and $\rho = 30$ mm by means of a perturbation model⁵⁸. Assuming that the thickness of the upper (extra-cerebral) layer is 10 mm, we can clearly see from Supplementary Figure SF3 (left column) that the photons detected at $\rho = 10$ mm propagate mainly in the extra-cerebral layer (above the dotted line in Supplementary Figure SF3), while

photons detected at $\rho = 30$ mm can pass through the extra-cerebral layer and reach the bottom (cerebral) layer (below the dotted line in Supplementary Figure SF1).

Finally, 3D Monte Carlo simulations of photon migration in the sheep head were run in a realistic mesh taken from the same animal to validate the depth sensitivity (e.g. maximum penetration depth) of the adopted configuration. The mesh was created segmenting data from Spin-Echo T1 and Fast Spin-Echo T2 (FSE) MRI neurocranium scans of the sample PECORA_978_MONTANA. The voxel resolution of each scan was 0.4688 mm. T1 data was used to segment the outer structure of the head (better contrast tissue/air) while T2 was used to segment the brain (sharper signal from the white matter). The segmentation was accomplished extrapolating binary masks (head and brain) with Fiji⁵⁹ and fed a meshing routine implemented via iso2mesh⁶⁰. The final mesh has 780,952 tetrahedral elements connecting 163,362 nodes. We took advantage of one of the most recent and accurate Monte Carlo simulation tools for the photon propagation, the Mesh-based Monte Carlo (MMC)⁶¹, to resolve the photon diffusion within the realistic sheep head mesh. Two simulations with source-detector distances of 10 mm and 30 mm were performed in the frontal lobe of the sheep head. All the MC simulations were performed on a computer running Windows 10 (64 bit) with an Intel Xeon E5-2670 (2.6G) 8-core processor and the memory of 64 GB. The simulation time was about 1.4 h with MMC method for 4×10^8 photons in each simulation.

From the above results, it can be concluded that the short optical channel ($\rho = 10$ mm) used in our study can only detect hemodynamic information from the extra-cerebral tissue of the sheep head, while the long optical channel ($\rho = 30$ mm) can detect hemodynamic information from both the extra-cerebral tissue and the cerebral tissue.



Supplementary Figure SF3. The CW sensitivity maps in a homogeneous slab (left column) and in a 3D realistic mesh of the sheep head (right column) detected at $\rho = 10$ mm (top row) and $\rho = 30$ mm (bottom row). The right images overlay the anatomical segmentations (light blue for the head and light red for the brain) on top of the corresponding T2-MRI scan (inverse gray map for contrast enhancement). The position of the supraorbital gyrus (SO) is also reported. The sensitivity maps show clearly deeper brain penetration for photons detected at $\rho = 30$ mm.

Supplementary Section S4 Validation of the two step fitting method

Very often fNIRS signals of cortical activity are contaminated by surface (e.g. scalp and skull) interferences, which may lead to confounding results and potentially to fake activations and artifacts. A common solution to eliminate these artifacts is to directly measure the extra-cerebral signal through a short separation channel and remove it from the signal originating from the cortical region by means of statistical and regression methods like general linear model or principal component analysis, or also wavelet decomposition⁶²⁻⁶⁶.

A limitation of this approaches is the fact that usually the short and long separation signals are both obtained by means of the modified Beer-Lambert law under the assumption that photons travel in a homogeneous volume^{66,67}.

We wanted to tackle the problem of discriminating superficial and cortical signal from a more physical point of view, by means of a multi-distance approach based on solution of the Diffusion Equation for photon migration in a two-layer geometry. This is similar to what already proposed with Monte Carlo instead of Diffusion Equation⁶⁸, and more generally to diffuse optical tomography approaches⁶⁹.

The fitting method adopted in this study is described in details in Section Materials and methods.

To verify the reliability of the proposed fitting method, we performed numerical simulations. Three different two-layer patterns of hemodynamic changes were generated using a physiologically relevant range of [O₂Hb] and [HHb] to mimic real changes in extra-cerebral and cerebral hemodynamics in sheep head during the fNIRS measurement. The steps of the forward modelling used to simulate hemodynamic changes are hereafter listed:

- The hemodynamic changes $\Delta[\text{O}_2\text{Hb}]^{\text{up}}(T)$ and $\Delta[\text{HHb}]^{\text{up}}(T)$ in up and down layer during stimulation period (considering a 10 s baseline period followed by 20 s stimulation, and 10 s recovery) were calculated⁷⁰ as a function of the experiment time T , and then converted into changes of the absorption coefficients in up and down layer $\Delta\mu_a^{\text{up}}(\lambda, T)$, $\Delta\mu_a^{\text{down}}(\lambda, T)$ using the Beer law⁴⁷.
- The absorption coefficients for the two layers were obtained by adding to $\Delta\mu_a^{\text{up}}(\lambda, T)$ and $\Delta\mu_a^{\text{down}}(\lambda, T)$ the baseline absorption coefficients $\mu_{a0}(\lambda)$, as obtained in Supplementary Section S2.
- The diffuse reflectance time courses at short $R_{\text{short}}(\lambda, T)$ and long $R_{\text{long}}(\lambda, T)$ source detector distance ($\rho_{\text{short}} = 10$ mm, $\rho_{\text{long}} = 30$ mm) were calculated using the two-layer solution of the photon Diffusion Equation, assuming the thickness of up layer $s = 10$

mm, and assuming that the scattering coefficient was constant and equal in both layers ($\mu_s^{\text{'up}}(\lambda, T) = \mu_s^{\text{'down}}(\lambda, T) = \mu_{s0}(\lambda)$).

- Finally, the time courses for the changes in optical density at short and long source detector distance were calculated from $R_{\text{short}}(\lambda, T)$ and $R_{\text{long}}(\lambda, T)$:

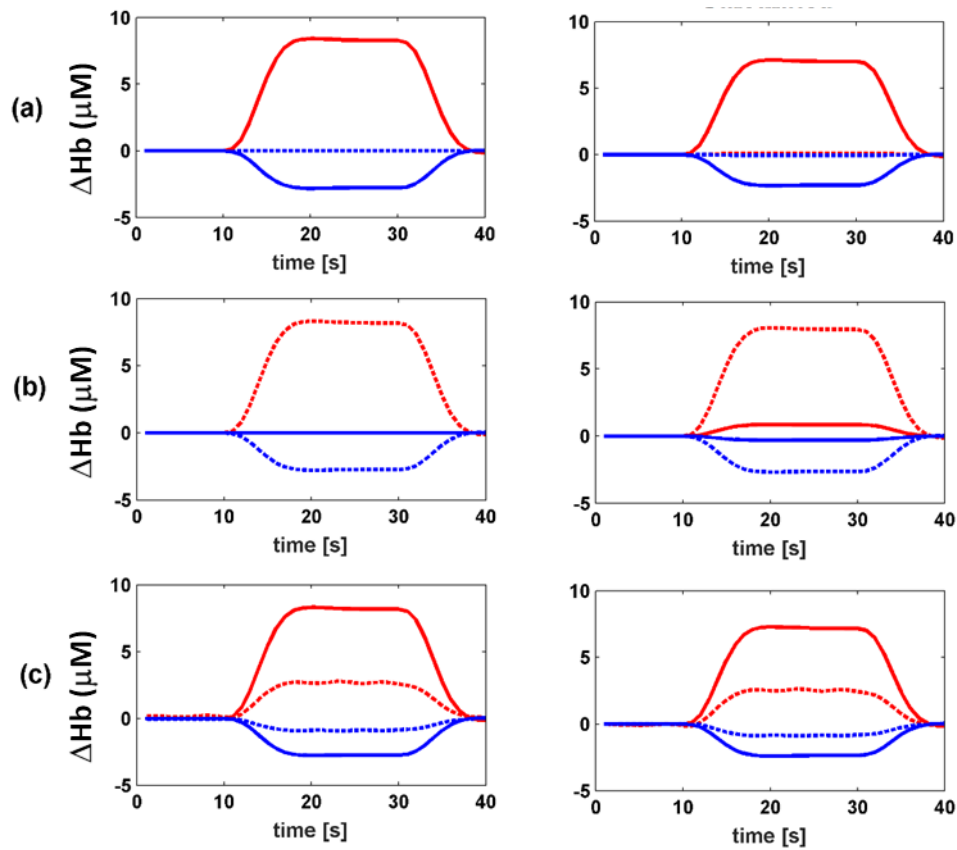
$$\Delta OD_{\text{short}}(\lambda, T) = \log_{10}[R_{\text{short}}(\lambda, T_0)/R_{\text{short}}(\lambda, T)]$$

$$\Delta OD_{\text{long}}(\lambda, T) = \log_{10}[R_{\text{long}}(\lambda, T_0)/R_{\text{long}}(\lambda, T)]$$

The simulated time courses for $[\Delta O_2Hb]$ and $[\Delta HHb]$ in the up and down layer for the three different response patterns are shown in Supplementary Figure SF4: a) only the bottom layer (solid line) has hemodynamic changes, while the upper layer (dashed line) has only noise (Supplementary Figure SF4a); b) only the upper layer has hemodynamic changes, while the bottom layer has only noise (Supplementary Figure SF4b); c) both layers have similar hemodynamic changes, but the bottom response is relatively stronger (Supplementary Figure SF4c).

The fitting method described in Section Materials and Methods was then used to estimate $[\Delta O_2Hb](T)$ and $[\Delta HHb](T)$ from the simulated $\Delta OD(\lambda, T)$, and results are shown in right column of Supplementary Figure SF4.

By comparing the simulated hemodynamic changes and the corresponding estimated hemodynamic changes, we can conclude that the used fitting method can effectively separate signals coming from the upper (extra-cerebral) layer and the bottom (cerebral) layer. The maximum error between the simulated and estimated $[\Delta O_2Hb]$ and $[\Delta HHb]$ for the three different response patterns is $<0.2 \mu M$ for the bottom layer and $<0.03 \mu M$ for the up layer. These small errors may be due to the use of Beer Lambert's law when $[\Delta O_2Hb]$ and $[\Delta HHb]$ were converted to ΔOD , which is valid on the assumption that the head is a homogeneous medium.



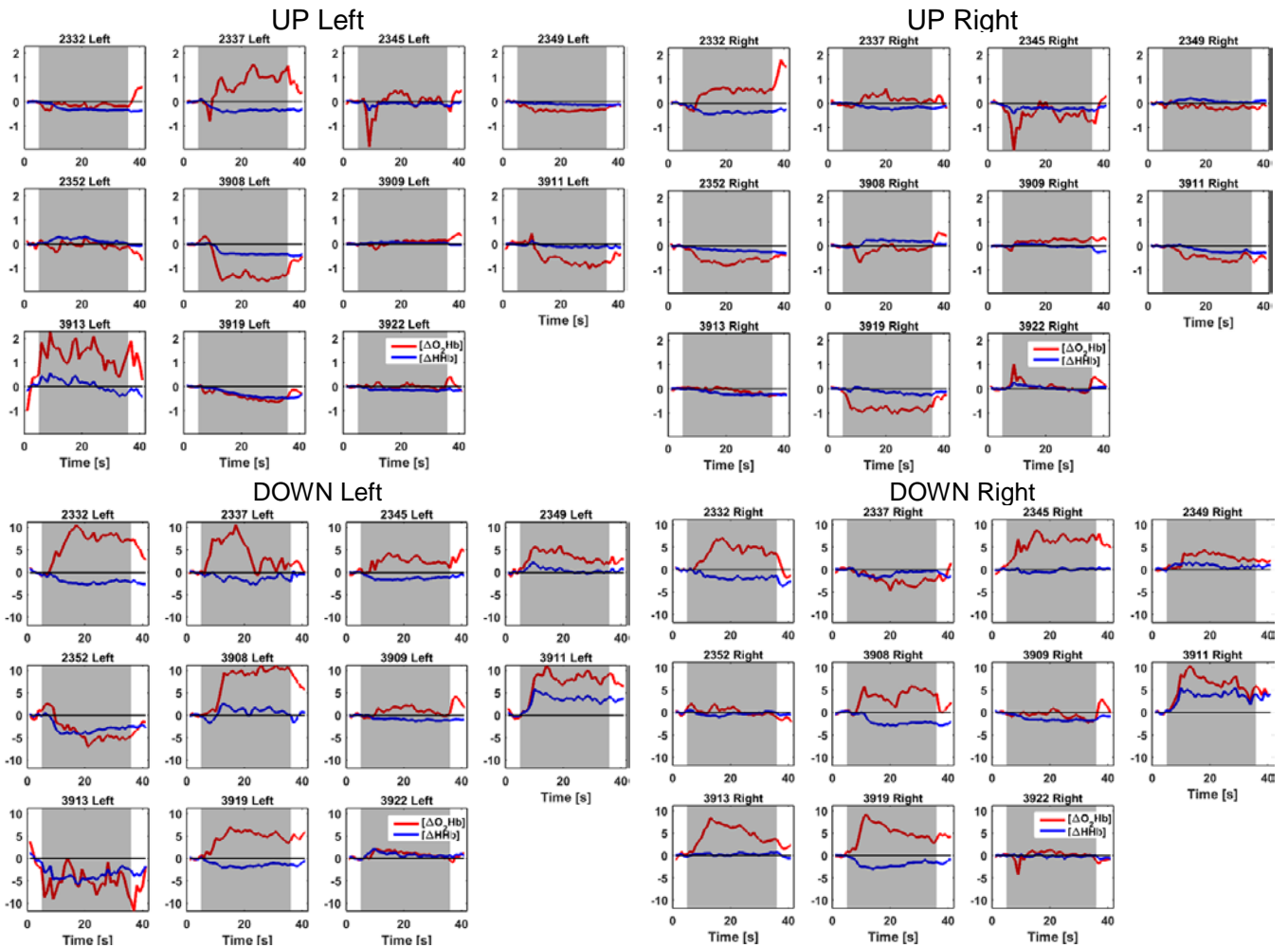
Supplementary Figure SF4. The simulated (left column) and estimated (right column) $[\Delta\text{O}_2\text{Hb}]$ (in red) and $[\Delta\text{HHb}]$ (in blue), in μM , for three different response patterns: (a) only the bottom layer (solid lines) has hemodynamic changes, while the upper layer (dashed lines) has only noise; (b) only the upper layer has hemodynamic changes and the bottom layer has only noise; (c) both layers have similar hemodynamic changes, but the bottom response is relatively larger.

Supplementary Section S5 Ethogram of sheep behavior

Supplementary Table ST2. Ethogram of sheep behavior.

Behavior	Description
Running	The sheep trots/gallops
Jumping	The sheep suddenly springs off the ground
Head shaking	The sheep shakes its head suddenly, violently and frequently either up/down or left/right
Chewing	The sheep works in the mouth with the teeth
Freezing	The sheep becomes rigid or motionless (standing still without moving) after the umbrella opening
Flight response	The sheep runs away after the umbrella opening

Supplementary Section S6 Block-average of hemoglobin changes in each sheep in the walking experiment



Supplementary Figure SF5. Block-average of $[\Delta\text{O}_2\text{Hb}]$ (red lines) and $[\Delta\text{HHb}]$ (blue lines), in μM , during the motor task for extra-cerebral (Up) tissue (top row) and cerebral (Down) tissue (bottom row) and for the left (left column) and right (right column) hemisphere in each sheep (sheep ID number on top of each panel). In every plot, the first 5 s are the baseline (sheep stand still), followed by 30 s walking (marked as gray area), and finally 5 s recovery period (sheep stand still). The horizontal black line in every sub-figure indicates the zero value.

Supplementary Section S7 Additional statistical analysis

Supplementary Table ST3. p-values of paired sample Student T-test comparing the hemodynamic response (i.e., oxygenated hemoglobin change [ΔO_2Hb] and deoxygenated hemoglobin change [ΔHHb]) in the baseline (0 - 5 s) and in the period (10 - 25 s) for all experiments. The symbol ‘-’ indicates that the p-value is not statistically significant ($p \geq 0.05$).

	UP				DOWN			
	left		right		left		right	
	ΔO_2Hb	ΔHHb						
Motor task	-	1.14E-08	2.05E-07	6.98E-08	1.22E-10	2.73E-09	1.92E-13	4.80E-09
Startling test (all sheep)	2.66E-08	-	1.04E-06	1.06E-03	1.39E-08	3.16E-04	1.92E-04	-
Startling test (Move group)	1.44E-05	-	6.06E-07	3.04E-03	2.44E-09	4.87E-05	4.35E-05	-
Startling test (Stand group)	-	8.38E-04	1.15E-02	7.29E-05	2.74E-02	1.16E-02	-	7.92E-08